Interface Focus

Interface Focus (2012) **2**, 378–386
doi:10.1098/rsfs.2012.0002

Dual functional selenium-substituted hydroxyapatite

Yanhua Wang, Jun Ma, Lei Zhou, Jin Chen, Yonghui Liu, Zhiye Qiu and Shengmin Zhang*

Advanced Biomaterials and Tissue Engineering Center, Huazhong University of Science and Technology, Wuhan 430074, People's Republic of China

Hydroxyapatite (HA) doped with trace elements has attracted much attention recently owing to its excellent biological functions. Herein, we use a facile co-precipitation method to incorporate selenium into HA by adding sodium selenite during synthesis. The obtained selenium-substituted HA products are needle-like nanoparticles which have size and crystallinity that are similar to those of the pure HA nanoparticles (HANs) when the selenium content is low. HANs are found to have the ability to induce the apoptosis of osteosarcoma cells, and the anti-tumour effects are enhanced after incorporation of selenium. Meanwhile, the nanoparticles can also support the growth of bone marrow stem cells. Furthermore, the flow cytometric results indicate that the apoptosis induction of osteosarcoma cells is caused by the increased reactive oxygen species and decreased mitochondrial membrane potential. These results show that the selenium-substituted HANs are potentially promising bone graft materials in osteosarcoma treatment due to their dual functions of supporting normal cell growth and inducing tumour cell apoptosis.

Keywords: hydroxyapatite; selenium; nanoparticles; malignant bone tumour; bone repair

1. INTRODUCTION

Hydroxyapatite (HA) is the main inorganic mineral in the hard tissues of humans and animals, including bone and tooth enamel [1]. In orthopaedic and maxillofacial clinical surgery, HA is often used as bone graft material to support bone growth and remodelling [2,3]. Furthermore, it is well known that HA in natural bone mineral contains various trace elements [4], such as magnesium [5], silicon [6,7] and zinc [8,9]. The trace elements play very important roles in bone formation and regeneration. Pure HA nanoparticles (HANs) modified with various cations/anions can be synthesized by an aqueous precipitation method [6,10–12]. Using precipitation methods, the trace elements can be easily incorporated into the HA lattice. HA materials with some trace elements can exert some special biological functions besides repairing bone defects. For instance, silicon-doped HA has been found to be able to promote rapid bone mineralization [6,13]. Recently, some complex composites containing HA have been designed to induce bone cancer cell apoptosis by magnetic hyperthermal therapy [14–16]. Meanwhile, these materials possess good biocompatibility and support bone regeneration [15,16]. Previous studies also demonstrate that apoptosis of various types of cancer cells can be induced by HANs, such as hepatoma [17] and gastric cancer [18] because of the nanosize effect. The cytotoxity caused by apoptosis induction is significantly increased when the particle size is smaller than 100 nm [17,19]. It is suggested that the cytotoxicity of nanoparticles has greatly limited their applications in clinic. For bone defect repairing, HANs more than 100 nm may have better compatibility and less cytotoxicity.

Osteosarcoma is a malignant primary bone tumour with a high mortality rate and a poor clinical prognosis in both children and adolescents [20]. After the osteosarcoma tumour tissues are treated by wide local resection in clinic, the defect void is often filled with bone graft materials [21,22]. The osteosarcoma is difficult to clean up and there is a high probability that the bone cancer will recur after resection. Mostly, chemoprevention therapy is needed even after the defect void has been repaired by the bone graft materials [22]. If the bone graft materials can both support bone regeneration and induce apoptosis of osteosarcoma cells, it will speed up the healing process and lower the risk of cancer recurrence. In this paper, the enhanced anti-tumour effects are studied by adding selenium to the HAN. The modified HAN can not only exert essential anti-tumour properties, but also have less toxicity than normal cells. There is much evidence that the selenium compounds possess anti-cancer properties [23–26]. Selenium can be incorporated into the HA lattice in the form of selenite ions [27]. The selenite ions have been found to induce the apoptosis of acute promyelocytic leukaemia NB4

---

*Author for correspondence (smzhang@mail.hust.edu.cn).

One contribution of 11 to a Theme Issue 'Biomaterials research in China'.

Received 7 January 2012
Accepted 4 March 2012

cells by the generation of reactive oxygen species (ROS) [24]. In addition, many organic/inorganic selenium compounds have been found capable of inducing apoptotic death of tumour cells [25,26].

In this paper, selenium-substituted HANs (SeHANs) have been synthesized by an aqueous co-precipitation method. The influence on the cellular growth of bone marrow mesenchymal stem cells (BMSCs) and MG63 (human osteosarcoma cell line) has carefully been studied. To comprehensively understand the intracellular mechanism, the ROS generation and mitochondrial membrane potential of MG63 cells after being treated by the nanoparticles have also been investigated.

2. MATERIAL AND METHODS

2.1. Chemical agents

Na_2SeO_3 was obtained from Tianjin Chemical Reagent Institute (China). $Ca(NO_3)_2{\cdot}4H_2O$ was purchased from the National Medicine Chemical Reagent Company (China). $(NH_4)_2HPO_4$ was obtained from Shanghai Regal Biotech Technology, Inc. (China). All these chemicals are of analytical grade. Dulbecco's modified Eagle medium (DMEM), foetal bovine serum (FBS), trypsin–EDTA, penicillin–streptomycin antibiotics were all purchased from Hyclone (USA). 2,7-Dichlorofluorescin-diacetate (DCFH-DA) was purchased from Amresco (USA). Rhodamine 123 dye and the cell growth determination kit (3-(4,5-dimethylthiazol-2-yl)-2,5-diphenyl tetrazolium bromide (MTT)-based) were obtained from Sigma (St Louis, MO, USA). The Annexin V-FITC/PI (fluorescein isothiocyanate/propidium iodide) apoptosis kit was purchased from Nanjing KeyGen Biotech. Co. Ltd. (China).

2.2. Synthesis of HANs and SeHANs

The stoichiometric HAN used in the experiments were prepared by an aqueous precipitation method [9,28]. Calcium nitrate and ammonium hydrogen phosphate were used as a source of Ca^{2+} and PO_4^{3-} ions, respectively. The molar ratio of Ca/P is 1.667 in the reaction and the pH value is kept at 10 by adding 25% ammonia solution. The SeHANs were produced by the addition of sodium selenite during synthesis. The phosphate salt used in the preparation was reduced according to the amount of sodium selenite added in the reaction. Briefly, the mixed solution (180 ml) of an appropriate amount of $(NH_4)_2HPO_4$ (the final concentration was 30, 29.8, 29.6 and 29.4 mM for HAN, SeHAN-1, SeHAN-2 and SeHAN-3, respectively) and Na_2SeO_3 (the final concentration was 0, 0.298, 0.592 and 0.882 mM, for HAN, SeHA-1, SeHAN-2 and SeHAN-3, respectively) was dropped into the $Ca(NO_3)_2{\cdot}4H_2O$ aqueous solution (50 mM, 180 ml) at 85°C under vigorous stirring. The white precipitate formed immediately and the suspension was aged at 85°C for 16 h. The pH value was kept at 10 by adding 25% ammonia solution during synthesis. After ageing, the products were centrifugated. The obtained precipitate was thoroughly washed with double-distilled water for five times in order to get rid of the physically adsorbed ions on the surface of nanoparticles. After that, the products were dried at 50°C overnight and ground into fine powders. All of the samples were used without sintering. Before cell culture, the nanoparticles were sterilized using ultraviolet light for 1 h and then suspended in the culture medium.

2.3. Physiochemical analysis

The atomic concentrations of elements (Ca, P and Se) in the products were measured by X-ray fluorescence (XRF) spectroscopy. The particle size of the obtained nanoparticles was measured by dynamic light scattering (DLS, Nano-ZS90, Malvern, UK). The particles were dispersed in double-distilled water by sonication for the DLS analysis. The morphology of the samples was examined by transmission electron microscopy (TEM, Tecnai G2 20, FEI, Holland). The nanoparticles were dispersed in ethanol by sonication and put on the copper grid with carbon film for TEM observation.

The crystal form and crystallinity were characterized by X-ray diffraction (XRD, X'Pert PRO, PANalytical B.V., The Netherlands). The data were recorded in the 2θ range from 10° to 60° using Cu-K_α radiation (40 mA, 40 kV) with a step size of $0.02^\circ\ s^{-1}$. The diffraction patterns were compared with the standard diffraction pattern of HA (PDF 09-0432). The crystallite size values along (002) were calculated using the Scherrer equation ($D = K\lambda/\beta \cos \Theta_\beta$, where λ is the wavelength, $K = 0.9$, Θ_β the angle of peak position and β the full width at half-maximum intensity in radians).

The characteristic functional groups of the samples were identified by Fourier transform infrared spectroscopy (FTIR, Vertex 70, Bruker, German). The FTIR spectra were recorded in the 4000–400 cm^{-1} region.

2.4. Cell culture and evaluation

The human BMSCs were purchased from the Chinese Center of Type Culture Collection in Wuhan University (Wuhan, China). The MG63 cells were provided by Tongji Medical College of Huazhong University of Science and Technology (Wuhan, China). Both cell lines were cultured in DMEM supplemented with 10% FBS, 100 units ml^{-1} penicillin and 100 mg ml^{-1} streptomycin at 37°C in a CO_2 incubator (95% relative humidity, 5% CO_2). The cell culture medium was changed every other day. The cells were cultured on a 48-well plate at an initial cell density of 2×10^6 cells ml^{-1}. After attachment for 24 h, the nanoparticles were added to the culture medium. The culture medium without any nanoparticles was used as control.

For morphological observation, the cells cultured for 48 h were stained using crystal violet dye. The cell number of BMSC and MG63 on the culture plates was estimated as follows at different time points. The cells were detached from the culture plate using trypsin–EDTA. A drop of cell suspension was applied on a haemocyte counting plate and the cells were stained using trypan blue dye. The density of viable cells (indicated by trypan blue dye) was measured under a microscope (100×). Each sample at each time point has three repetitions.

Table 1. Elemental analysis and particle size of the prepared samples.

sample name	nominal Se/P (%)	measured Se/P (%)	nominal Ca/(P + Se)	measured Ca (P + Se)	particle size (nm)
HAN	0	0	1.667	1.68 ± 0.02	167 ± 14
SeHAN-1	1.0	0.4 ± 0.3	1.661	1.59 ± 0.08	184 ± 6
SeHAN-2	2.0	0.7 ± 0.2	1.656	1.61 ± 0.06	181 ± 12
SeHAN-3	3.0	1.1 ± 0.3	1.651	1.58 ± 0.08	183 ± 6

2.5. Induction of apoptosis on MG63

The viability of MG63 cells was assessed *in vitro* with a cell growth determination kit (MTT-based) [17]. Nanoparticles including SeHANs with different selenium concentrations and pure HANs were added to the cell culture medium (DMEM) for 48 h at 37°C. The control group was exposed only to DMEM. Each condition was tested with six repetitions.

The Annexin V-FITC/PI double stain assay was performed to further confirm the induction of apoptosis on MG63 cells. After culturing for 48 h, Annexin V-FITC (5 μl) and PI (5 μl) were added to the suspension, and incubated in the dark for 15 min. After that, the samples were immediately analysed with flow cytometry (Beckman Coulter Cytomics FC500, USA). Excitation wave was set at 488 nm, and the emitted green fluorescence of Annexin V and red fluorescence of PI were collected using 525 and 575 nm band pass filters, respectively.

The ROS generation was measured by fluorescence of 2′,7′-dichlorofluorescein (DCF) originated from DCFH-DA using flow cytometry. Cells were harvested by centrifugation, washed twice with ice-cold phosphate buffer solution (PBS), and suspended in ice-cold PBS (1×10^6 cells ml^{-1}). Then, cell suspension (500 μl) was placed into a polyethylene tube and loaded with DCFH-DA to a final concentration of 20 μM, and incubated at 37°C for 15 min. After adding HAN or SeHAN-3 (200 μg ml^{-1}), cells were incubated at 37°C for 30 min. Then, ROS generation was measured by the fluorescence intensity (FL-1, 530 nm) of 10 000 cells with flow cytometry (Beckman Coulter Cytomics FC500, USA). The mean fluorescence intensities were obtained by histogram statistics using the cytometer CXP software.

To probe the changes of mitochondrial transmembrane potential after the HAN and SeHAN (200 μg ml^{-1}) treatments for 48 h, the cell permeable cationic dye rhodamine 123 was used to stain the cells [29]. The alteration of the mitochondrial membrane potential was investigated by the fluorescence intensity (ex, 488–505 nm; em, 515–575 nm) with flow cytometry. For each experiment, 5000 events per sample were recorded.

2.6. Statistical analysis

All experiments were carried out at least in triplicate and data were expressed as mean ± standard deviation. Statistical analysis was performed using SPSS v. 13.0. The difference between two groups was analysed by two-tailed Student's *t*-test and that among three or more groups was analysed by one-way analysis of variance (ANOVA). A difference with $^{*}p < 0.05$ or $^{**}p < 0.01$ (double asterisks) was considered statistically significant.

3. RESULTS

3.1. Physicochemical characterization

3.1.1. Se/P molar ratios

During the preparation of SeHAN, sodium selenite was used as the source of selenium. The Ca, P and Se contents in HANs and SeHANs were detected by XRF. The Se/P and Ca/(Se + P) molar ratios were calculated according to the reaction recipe (nominal value) and the XRF measurements, separately. As shown in table 1, the Se/P molar ratios in the HAN and SeHAN samples increase along with the selenium content added to the reaction mixture. However, the Se/P molar ratios measured by XRF are always lower than the nominal ratios.

3.1.2. Particle size and morphology

The particles were suspended in double-distilled water for DLS particle size analysis. The obtained particle size is shown in table 1. According to the results, the particle size of SeHAN becomes a little larger than that of HAN. By using TEM, the nanoparticles were found to be bundles of needles, as shown in figure 1. These nanoparticles have a width of 20–30 nm and a length of 150–200 nm. This suggests that the selenium substitution in HA has no significant influence on the particle morphology.

3.1.3. Crystallinity and functional groups

All of the samples have no obvious difference in the XRD patterns as shown in figure 2*a*. The results indicate that the selenium substitution has not changed the crystallinity and crystal structures. No secondary phase was detected. The crystallite mean size along (002) ($D_{(002)}$), as calculated using the Scherrer equation, varied from 17 nm (HAN) to 20 nm (SeHAN-1). The SeHANs have similar crystallite sizes when the Se/P molar ratios vary from 0.01 to 0.03.

FTIR was conducted to further verify the selenium substitution process, as shown in figure 2*b*. The peaks corresponding to the phosphate (PO_4^{3-}) groups 1092, 1037, 603 and 567 cm^{-1} and to the hydroxyl (OH^-) groups 1568 and 3570 cm^{-1} were observed. The peaks of 1460 and 1420 cm^{-1} owing to the carbonate (CO_3^{2-}) groups indicate that some CO_2 gas in the atmosphere has been introduced during preparation [5]. Moreover, the additional peak in SeHANs detected

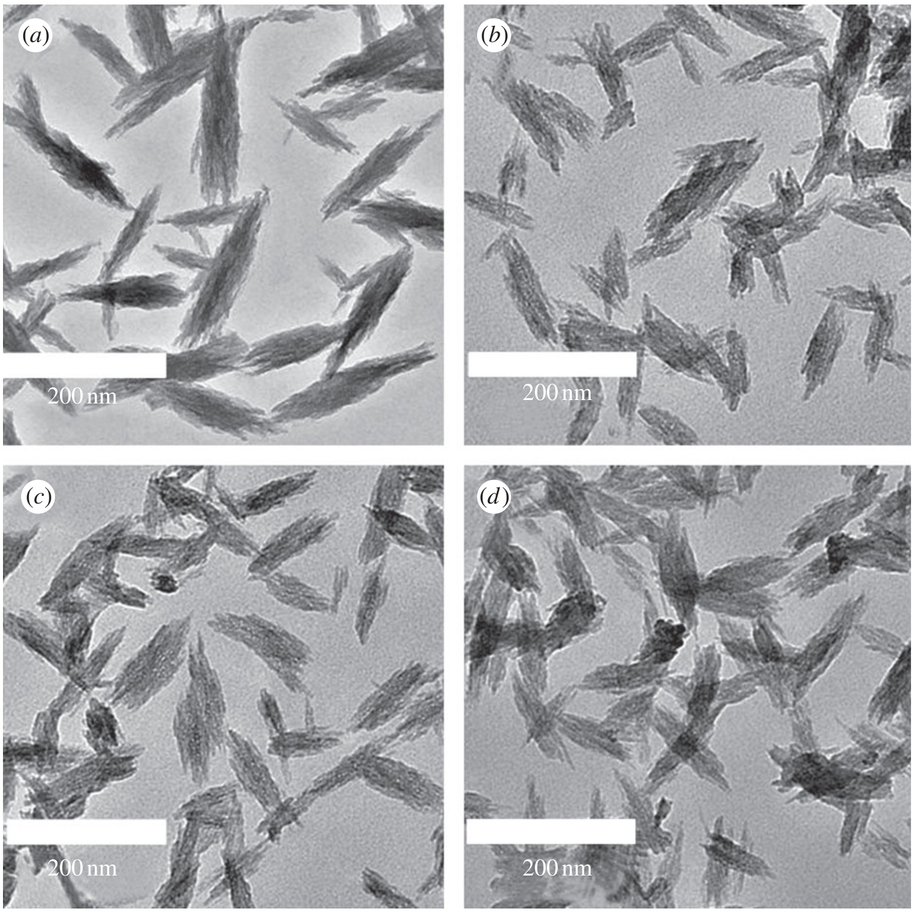

Figure 1. Typical TEM micrographs: (*a*) HAN, (*b*) SeHAN-1, (*c*) SeHAN-2 and (*d*) SeHAN-3.

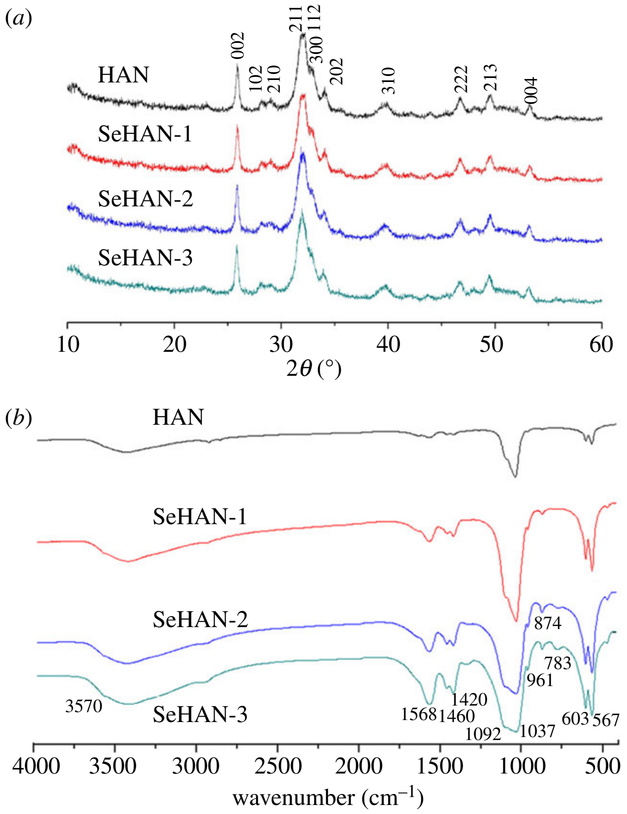

Figure 2. (*a*) X-ray diffraction (XRD) patterns with the major crystalline planes of hydroxyapatite. (*b*) Fourier transform infrared spectroscopy (FTIR) analysis.

at 783 cm^{-1} can be assigned to the selenite (SeO_3^{2-}) groups [27]. The peak at 874 cm^{-1} is possibly caused by both carbonate groups and selenite groups. By comparison, the peaks belonging to the selenite groups and the carbonate groups become stronger along with the selenium content.

It is well known that the chemical formula of the pure HA is $Ca_{10}(PO_4)_6(OH)_2$. According to the above results, the chemical formula of the synthetic SeHAN can be written as $Ca_x(PO_4)_{6-y}(SeO_3)_y\ (CO_3)_z(OH)_{2x+y-18-2z}$ with $0 < x < 10$, $0 < y < 0.1$, $0 < z < 1$. The selenite group is divalent and has less negative charge than the trivalent phosphate group. Due to the charge compensating mechanism, more hydroxyl groups are possibly replaced by carbonate groups. As a result of this the content of carbonate groups increases with the content of selenite groups. For instance, the chemical formula of SeHAN-3 is proposed as $Ca_{9.38}(PO_4)_{5.94}(SeO_3)_{0.065}(CO_3)_z\ (OH)_{0.81-2z}$ $(0 < z < 0.4)$.

3.2. Cell culturing results

3.2.1. Cell growth and viability

In figure 3, BMSCs have no obvious difference after adding HAN and SeHAN-3 to the culture medium. Meanwhile, MG63 cells treated by HAN and SeHAN-3 presented different levels of cell viability compared with the control group. It is obvious that SeHAN-3 has shown the highest level of toxicity on MG63 cells. From the cell-counting results in figure 4, it is indicated that

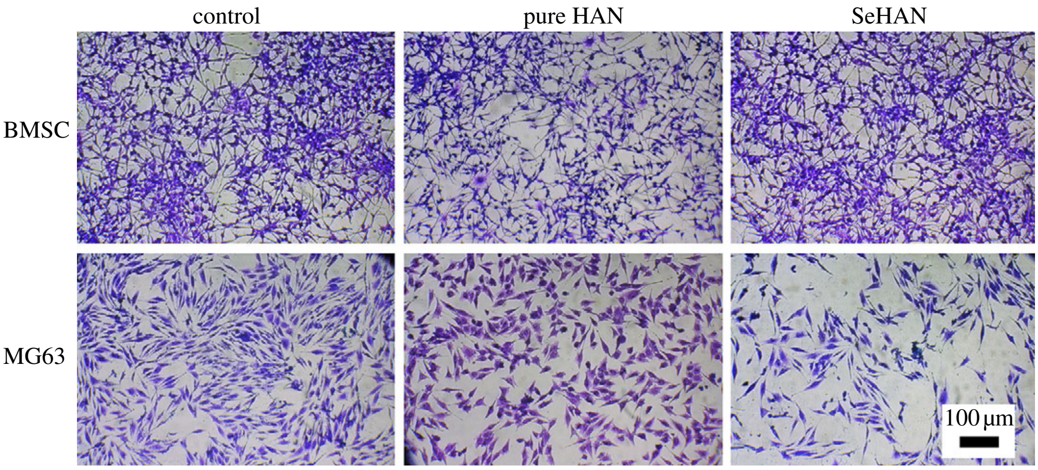

Figure 3. Cells stained using crystal violet dye after culturing for 48 h. Control refers to no addition of nanoparticles.

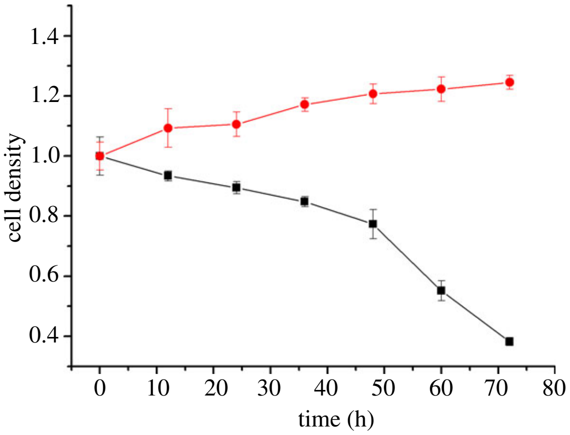

Figure 4. Cell density results of BMSCs and MG63 after adding SeHAN-3. The viable cells were stained using trypan blue at different time points. Black solid line with squares, MG63; red solid line with circles, BMSCs.

the cell density increased for BMSCs and decreased for MG63 after adding SeHAN-3 to the culture medium. After 72 h, less than 40% MG63 cells survived. From the MTT results in figure 5*a*, SeHAN-3 has the highest growth-inhibiting activity on MG63 cells. The cell viability has a negative linear correlation with the selenium content in the nanoparticles. As shown in figure 5*b*, the cell viability of MG63 cells decreased when the SeHAN-3 concentration increased. The cell viability has decreased by about 40% when the concentration of SeHAN-3 reached 200 $\mu g\ ml^{-1}$.

3.2.2. Induction of apoptosis in MG63 cells

To further quantify the percentage of cell death and apoptosis, Annexin-V and PI staining assay was performed. Both apoptotic cells and necrotic cells were stained by Annexin-V, while only the necrotic cells were stained by PI [17]. As shown in figure 6*a*, it is possible to distinguish and quantitatively analyse non-apoptotic or live cells (Annexin V-FITC negative and PI negative, C3 area), early apoptotic cells (Annexin-V FITC positive and PI negative, C4 area), late apoptotic cells (Annexin-V FITC positive and PI positive, C2 area). Very small quantities of apoptotic cells (C2 and C4 areas) were detected in the control group. After being treated by HAN and SeHAN-3, more dots were seen in the C2 and C4 areas, so the cell death induced by HAN and SeHAN-3 was mainly caused by apoptosis. The average apoptosis percentage of the control, HAN and SeHAN-3 are 1.85%, 16.15% and 27.11%, respectively (figure 6*b*). The apoptotic percentage of MG63 cells treated by SeHAN-3 is nearly 70% higher than that treated by HAN ($p < 0.01$). It is obvious that SeHAN-3 show more efficiency in inducing MG63 osteosarcoma cells apoptosis than HAN.

3.2.3. Generation of ROS in MG63 cells

To explore the underlying mechanisms of cell apoptosis induction by SeHAN, ROS generation was studied. The intracellular generation of ROS is often detected using DCFH-DA. Inside the cell, DCFH-HA is cleaved to form DCFH, which is then oxidized to dichlorofluorescein (DCF) by ROS [13]. Fluorescence emission by DCF can be monitored by a flow cytometer which indicates the ROS production level inside the cells. Both HAN and SeHAN-3 greatly increased the DCF fluorescence intensity in MG63 cells compared with the control group. It is indicated that both HAN and SeHAN-3 can increase intracellular ROS generation. Moreover, the DCF fluorescence of the SeHAN-3 group was slightly higher than that of the HAN group ($p < 0.05$, figure 7*a*). It is indicated that the selenium substitution leads to the increased level of intracellular ROS in the MG63 cells.

3.2.4. Effect of mitochondrial membrane potential in MG63 cells

Previous studies considered mitochondria as a potential source for ROS generation [13]. ROS generation could cause the collapse of mitochondrial membrane potential and lead to cell apoptosis. Herein, we investigated the mitochondrial membrane potential by rhodamine 123 staining. In the apoptotic cells, mitochondrial integrity is lost and the permeability transition pore channels open. The intensity of intracellular rhodamine 123 fluorescence decreases in apoptotic cells. As shown in figure 7*b*, both HAN and SeHAN-3 treatments decreased the fluorescence intensity of intracellular rhodamine 123, which indicated that the mitochondrial membrane potential was lost. In addition, the fluorescence intensity of the SeHAN-3 group was significantly lower than that of the HAN group ($p < 0.01$). This indicates that the SeHAN-3 treatments could cause significant loss of mitochondrial transmembrane potential.

4. DISCUSSION

Over recent years, studies about the molecular changes in the internal or external cellular environment have emerged as a topic of rapidly expanding scientific interest [18,30–33]. Apoptosis, as an important way to maintain the cellular homeostasis between cell division and cell death, has received a lot of attention [26,34–36]. A defect of apoptosis has been implicated in various human cancers [23,35–37]. And recently, many attempts have been made to develop some new anti-cancer agents via the induction of apoptosis [15,20]. HA is widely used as a kind of bone graft material for the surgical treatments of bone defects, such as bone trauma or osteosarcoma extraction [20]. In this study, SeHANs have been proposed as a novel biomaterial for osteosarcoma therapy. During preparation, sodium selenite was used to introduce selenite groups into HANs. The selenium concentration in the final products is found to have a linear correlation with the addition of sodium selenite in the reaction. The sodium ions may also be introduced into the final products. The XRD results show that the synthetic powders are monophasic and the main peaks are the same as that of HA.

The addition of selenite ions to HANs enhances the inhibiting effect of the nanoparticles to MG63 cell growth. At the same time, the nanoparticles are safe to use normal BMSCs. The results show that SeHANs have dual biological functions (inhibiting tumour cells and supporting bone cells) which may have promising potential applications in clinic.

It is known that the cellular response to new implant materials is determined by their physical and chemical properties [38]. The physical characteristics including size, morphology and crystallinity can affect the cellular behaviours [17,39]. The HANs and SeHANs used in this study have similar morphology, crystal size and crystallinity. These nanoparticles only have a little difference because less than 3 per cent of phosphate ions are considered to be replaced by selenite ions. The selenite ions are found to be able to diffuse into HA crystals to replace phosphate groups by an exchange process [27]. It is considered that the HA lattice is easy to accept the selenite ions. Because the washing procedure was thoroughly conducted, the adsorbed selenite ions on the particle surface might be ignored during experiments. However, other techniques are needed to identify the crystal structure of the synthetic SeHANs, such as solid state nuclear magnetic resonance [7,40].

In this paper, we focused on studying the cellular response of SeHANs. Previous studies show that both selenite salts and HANs are toxic to cancer cells owing to the induction of apoptosis [17,24]. In this study, the synthetic SeHANs were found to be taken up by the tumour cells in the same way as HANs (data not shown). The uptake process of HAN was described in the previous publication [17]. The present results demonstrate that the cell death induced by SeHANs is mainly caused by apoptosis induction. Apoptotic cells can be found in the HAN-treated group and the percentage of apoptotic cells is 16.2 per cent, which is in accordance with the previous results [17]. Furthermore, SeHANs show enhanced efficiency in inducing MG63 cell apoptosis compared with HANs. The cell viability of MG63 is found to have a negative correlation with the selenium content in SeHANs.

In mammal cells, ROS are produced from many intracellular sources, such as mitochondrial respiration, xanthine oxidase, nicotinamide adenine dinucleotide phosphate oxidase, microsomes and peroxisomes [41]. They are elevated under various external stimuli. ROS can induce cell death by themselves or act as intracellular messengers during cell death. And recently, the generation of intracellular ROS is found to induce apoptosis, caspase activation and cytochrome c release [34,37,42–44]. Therefore, the role of ROS is considered as the upstream signal to induce apoptosis and caspase activation in the MG63 cells. The present results indicate that SeHANs have induced higher ROS generation level in the MG63 cells. The SeHAN may affect the intracellular sources of ROS generation. In addition, SeHANs may interact with some intracellular molecules and induce the disruption of important antioxidant molecules such as glutathione (GSH), *N*-acetylcysteine (NAC) and other thioredoxin [45]. The apoptosis rates increased nearly 70 per cent after the selenium substitution in HANs; however, the ROS production increased only a little. The apoptosis rates induced by the selenium substitution in HANs seem to have no direct correlation with the ROS production [46].

Another factor is considered to have direct relations in the cell apoptosis after the selenium substitution. Mitochondrial dysfunction results in a rise in intracellular calcium concentration, release of cytochrome c and the loss of the mitochondrial membrane potential, which will activate downstream events in the apoptotic process, such as the caspase cascade [18,26,47,48]. The previous study demonstrates that the apoptotic pathway of HAN-induced apoptosis is mediated through the mitochondrial-dependent and caspase-dependent pathways [18]. Furthermore, the caspase-9-dependent intrinsic apoptotic pathway plays a role in the interaction between the osteosarcoma cells and HANs [20]. The osteosarcoma cell apoptosis induced by the calcium and phosphate pairs exhibited remarkable changes in the mitochondrial membrane potential. The present results were consistent with these findings. Both HANs and SeHANs greatly impaired the mitochondrial function, leading to the loss of mitochondrial membrane potential, which eventually contributed to the cell apoptosis. The selenium in SeHANs can further decrease the mitochondrial membrane potential compared with HANs. Because of this, higher apoptotic percentage of MG63 cells was obtained by the selenium substitution.

5. CONCLUSIONS

In this study, SeHANs having size and morphology similar to those of HANs were synthesized by an

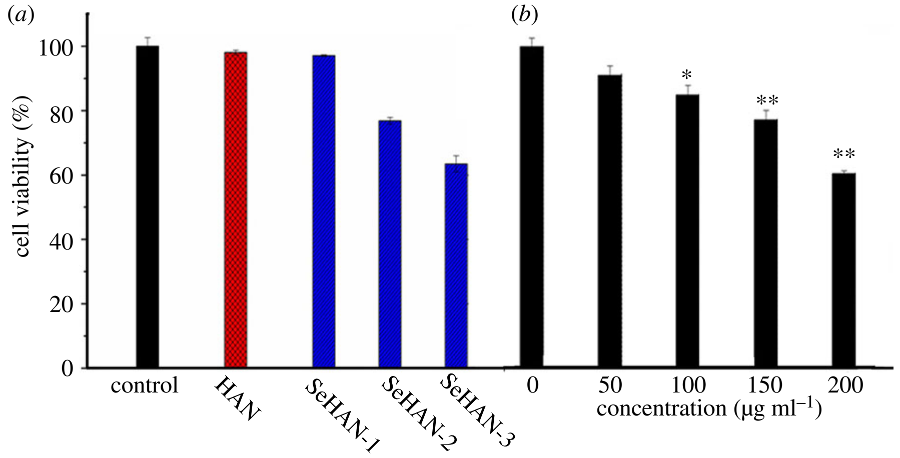

Figure 5. Cell viability of MG63 by MTT assay after 48 h of incubation (*a*) treated by HAN, SeHAN-1, SeHAN-2 and SeHAN-3, and (*b*) treated by different concentrations of SeHAN-3. The culture medium without nanoparticles is used as control.

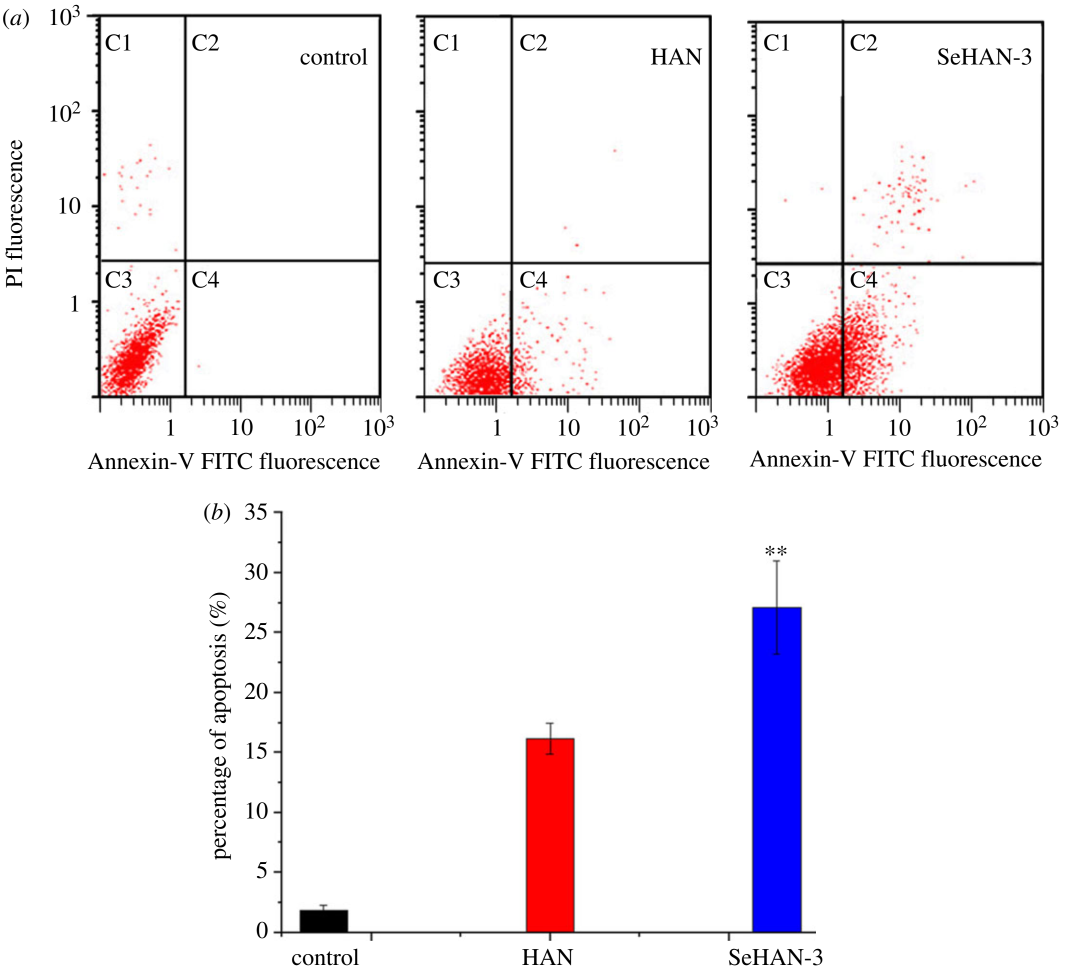

Figure 6. Flow cytometric analysis: (*a*) representative dot plots of Annexin V/PI staining of MG63 cells untreated (control) and treated by HAN and SeHAN-3 at 200 μg ml^{-1}, and (*b*) comparison of the effect of HAN and SeHAN-3 on the percentage of apoptotic MG63 cells.

aqueous precipitation method. The cell culturing experiments indicated that the cytotoxicity and apoptosis-inducing effect of HANs were significantly enhanced by the addition of selenium into the HA structure. According to the results, the apoptosis-induction effect of SeHANs is suggested to be caused by the activation of the intrinsic mitochondrial apoptotic pathway. This work provides strong evidence that SeHANs have the potential to be used as promising dual functional bone graft materials that can not only

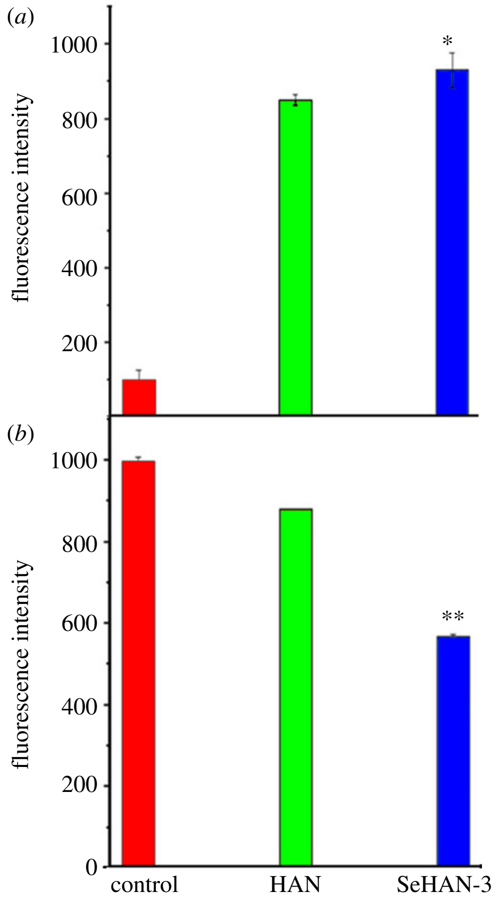

Figure 7. Flow cytometric analysis in MG63 cells: (*a*) ROS generation indicated by the DCF fluorescence and (*b*) mitochondrial membrane potential indicated by rhodamine 123 fluorescence.

support the bone regeneration, but also decrease the osteosarcoma recurrence possibility.

This work was supported by National Basic Research Program of China (grant no. 2012CB933601), National Natural Science Foundation of China (grant nos. 81071263, 30870624), International S&T Cooperation Program of China (grant no. 0102011DFA31430) and National High Technology Research and Development Program of China (grant no. 2011 AA03105).

REFERENCES

1 Rensberger, J. M. & Watabe, M. 2000 Fine structure of bone in dinosaurs, birds and mammals. *Nature* **406**, 619–622. (doi:10.1038/35020550)

2 Montufar-Solis, D., Nguyen, H. C., Nguyen, H. D., Horn, W. N., Cody, D. D. & Duke, P. J. 2004 Using cartilage to repair bone: an alternative approach in tissue engineering. *Ann. Biomed. Eng.* **32**, 504–509. (doi:10.1023/B:ABME.0000017546.29064.fc)

3 Allori, A. C., Sailon, A. M. & Warren, S. M. 2008 Biological basis of bone formation, remodeling, and repair-part. I. Biochemical signaling molecules. *Tissue Eng. Part B Rev.* **14**, 259–273. (doi:10.1089/ten.teb.2008.0082)

4 Elliott, J. C. 1994 *Structure and chemistry of the apatites and other calcium orthophosphates.* Amsterdam, The Netherlands: Elsevier.

5 Laurencin, D. *et al.* 2011 Magnesium incorporation into hydroxyapatite. *Biomaterials* **32**, 1826–1837. (doi:10.1016/j.biomaterials.2010.11.017)

6 Patel, N., Best, S. M., Bonfield, W., Gibson, I. R., Hing, K. A., Damien, E. & Revell, P. A. 2002 A comparative study on the *in vivo* behavior of hydroxyapatite and silicon substituted hydroxyapatite granules. *J. Mater. Sci. Mater. Med.* **13**, 1199–1206. (doi:10.1023/A:1021114710076)

7 Gomes, S., Renaudin, G., Mesbah, A., Jallot, E., Bonhomme, C., Babonneau, F. & Nedelec, J. M. 2010 Thorough analysis of silicon substitution in biphasic calcium phosphate bioceramics: a multi-technique study. *Acta Biomater.* **6**, 3264–3274. (doi:10.1016/j.actbio.2010.02.034)

8 Milachowski, K., Moschinski, D., Jaeschock, R. & Kaschner, A. 1980 The influence of zinc on bone healing in rats. *Arch. Orthop. Trauma Surg.* **96**, 17–21. (doi:10.1007/BF01246137)

9 Ren, F., Xin, R., Ge, X. & Leng, Y. 2009 Characterization and structural analysis of zinc-substituted hydroxyapatites. *Acta Biomater.* **5**, 3141–3149. (doi:10.1016/j.actbio.2009.04.014)

10 Koutsopoulos, S. 2002 Synthesis and characterization of hydroxyapatite crystals: a review study on the analytical methods. *J. Biomed. Mater. Res.* **62**, 600–612. (doi:10.1002/jbm.10280)

11 de Lima, I. R., Alves, G. G., Soriano, C. A., Campaneli, A. P., Gasparoto, T. H., Ramos Jr, E. S., de Sena, L. A., Rossi, A. M. & Granjeiro, J. M. 2011 Understanding the impact of divalent cation substitution on hydroxyapatite: an *in vitro* multiparametric study on biocompatibility. *J. Biomed. Mater. Res. A* **98A**, 351–358. (doi:10.1002/jbm.a.33126)

12 Lim, P. N., Tay, B. Y., Chan, C. M. & Thian, E. S. 2012 Synthesis and characterization of silver/silicon-cosubstituted nanohydroxyapatite. *J. Biomed. Mater. Res. B Appl. Biomater.* **100B**, 285–291. (doi:10.1002/jbm.b.31951)

13 Balamurugan, A., Rebelo, A. H., Lemos, A. F., Rocha, J. H., Ventura, J. M. & Ferreira, J. M. 2008 Suitability evaluation of sol–gel derived Si-substituted hydroxyapatite for dental and maxillofacial applications through *in vitro* osteoblasts response. *Dent. Mater.* **24**, 1374–1380. (doi:10.1016/j.dental.2008.02.017)

14 Veiseh, O., Gunn, J. W., Kievit, F. M., Sun, C., Fang, C., Lee, J. S. & Zhang, M. 2009 Inhibition of tumor-cell invasion with chlorotoxin-bound superparamagnetic nanoparticles. *Small* **5**, 256–264. (doi:10.1002/smll.200800646)

15 Hou, C. H., Hou, S. M., Hsueh, Y. S., Lin, J., Wu, H. C. & Lin, F. H. 2009 The *in vivo* performance of biomagnetic hydroxyapatite nanoparticles in cancer hyperthermia therapy. *Biomaterials* **30**, 3956–3960. (doi:10.1016/j.biomaterials.2009.04.020)

16 Andronescu, E., Ficai, M., Voicu, G., Ficai, D., Maganu, M. & Ficai, A. 2010 Synthesis and characterization of collagen/hydroxyapatite: magnetite composite material for bone cancer treatment. *J. Mater. Sci. Mater. Med.* **21**, 2237–2242. (doi:10.1007/s10856-010-4076-7)

17 Yuan, Y., Liu, C., Qian, J., Wang, J. & Zhang, Y. 2010 Size-mediated cytotoxicity and apoptosis of hydroxyapatite nanoparticles in human hepatoma HepG2 cells. *Biomaterials* **31**, 730–740. (doi:10.1016/j.biomaterials.2009.09.088)

18 Chen, X., Deng, C., Tang, S. & Zhang, M. 2007 Mitochondria-dependent apoptosis induced by nanoscale hydroxyapatite in human gastric cancer SGC-7901 cells. *Biol. Pharm. Bull.* **30**, 128–132. (doi:10.1248/bpb.30.128)

19 Theiszova, M., Jantova, S., Letasiova, S., Palou, M. & Cipak, L. 2008 Cytotoxicity of hydroxyapatite,

fluorapatite and fluor-hydroxyapatite: a comparative *in vitro* study. *Neoplasma* **55**, 312–316.

20 Shi, Z., Huang, X., Liu, B., Tao, H., Cai, Y. & Tang, R. 2010 Biological response of osteosarcoma cells to size-controlled nanostructured hydroxyapatite. *J. Biomater. Appl.* **25**, 19–37. (doi:10.1177/0885328209339396)

21 Yoshida, Y., Osaka, S. & Tokuhashi, Y. 2009 Clinical experience of novel interconnected porous hydroxyapatite ceramics for the revision of tumor prosthesis: a case report. *World J. Surg. Oncol.* **7**, 76. (doi:10.1186/1477-7819-7-76)

22 Meyers, P. A. *et al.* 2011 Addition of pamidronate to chemotherapy for the treatment of osteosarcoma. *Cancer* **117**, 1736–1744. (doi:10.1002/cncr.25744)

23 Letavayova, L., Vlckova, V. & Brozmanova, J. 2006 Selenium: from cancer prevention to DNA damage. *Toxicology* **227**, 1–14. (doi:10.1016/j.tox.2006.07.017)

24 Guan, L., Han, B., Li, Z., Hua, F., Huang, F., Wei, W., Yang, Y. & Xu, C. 2009 Sodium selenite induces apoptosis by ROS-mediated endoplasmic reticulum stress and mitochondrial dysfunction in human acute promyelocytic leukemia NB4 cells. *Apoptosis* **14**, 218–225. (doi:10.1007/s10495-008-0295-5)

25 Jackson, M. I. & Combs Jr, G. F. 2008 Selenium and anticarcinogenesis: underlying mechanisms. *Curr. Opin. Clin. Nutr. Metab. Care* **11**, 718–726. (doi:10.1097/MCO.0b013e3283139674)

26 Zhou, J., Cheng, G., Tang, H. F. & Zhang, X. 2011 Novaeguinoside II inhibits cell proliferation and induces apoptosis of human brain glioblastoma U87MG cells through the mitochondrial pathway. *Brain Res.* **1372**, 22–28. (doi:10.1016/j.brainres.2010.11.093)

27 Monteil-Rivera, F., Fedoroff, M., Jeanjean, J., Minel, L., Barthes, M. G. & Dumonceau, J. 2000 Sorption of selenite (SeO(3)(2-)) on hydroxyapatite: an exchange process. *J. Colloid Interface Sci.* **221**, 291–300. (doi:10.1006/jcis.1999.6566)

28 Gillespie, P., Wu, G., Sayer, M. & Stott, M. J. 2010 Si complexes in calcium phosphate biomaterials. *J. Mater. Sci. Mater. Med.* **21**, 99–108. (doi:10.1007/s10856-009-3852-8)

29 Darzynkiewicz, Z., Staiano-Coico, L. & Melamed, M. R. 1981 Increased mitochondrial uptake of rhodamine 123 during lymphocyte stimulation. *Proc. Natl Acad. Sci. USA* **78**, 2383–2387. (doi:10.1073/pnas.78.4.2383)

30 Gallo, D., Jacquot, Y., Laurent, G. & Leclercq, G. 2008 Calmodulin, a regulatory partner of the estrogen receptor alpha in breast cancer cells. *Mol. Cell Endocrinol.* **291**, 20–26. (doi:10.1016/j.mce.2008.04.011)

31 Leong, K. W. & Adler, A. F. 2010 Emerging links between surface nanotechnology and endocytosis: impact on nonviral gene delivery. *Nano Today* **5**, 553–569. (doi:10.1016/j.nantod.2010.10.007)

32 Hanifi, A., Fathi, M. H., Sadeghi, H. M. & Varshosaz, J. 2010 Mg^{2+} substituted calcium phosphate nano particles synthesis for non viral gene delivery application. *J. Mater. Sci. Mater. Med.* **21**, 2393–2401. (doi:10.1007/s10856-010-4088-3)

33 Vandiver, J., Dean, D., Patel, N., Bonfield, W. & Ortiz, C. 2005 Nanoscale variation in surface charge of synthetic hydroxyapatite detected by chemically and spatially specific high-resolution force spectroscopy. *Biomaterials* **26**, 271–283. (doi:10.1016/j.biomaterials.2004.02.053)

34 Hildeman, D. A., Mitchell, T., Teague, T. K., Henson, P., Day, B. J., Kappler, J. & Marrack, P. C. 1999 Reactive oxygen species regulate activation-induced T cell apoptosis. *Immunity* **10**, 735–744. (doi:10.1016/S1074-7613(00)80072-2)

35 Perlot Jr, R. L., Shapiro, I. M., Mansfield, K. & Adams, C. S. 2002 Matrix regulation of skeletal cell apoptosis. II. Role of Arg-Gly-Asp-containing peptides. *J Bone Miner Res* **17**, 66–76. (doi:10.1359/jbmr.2002.17.1.66)

36 Saunders, R., Szymczyk, K. H., Shapiro, I. M. & Adams, C. S. 2007 Matrix regulation of skeletal cell apoptosis. III. Mechanism of ion pair-induced apoptosis. *J. Cell Biochem.* **100**, 703–715. (doi:10.1002/jcb.21001)

37 Jung, U., Zheng, X., Yoon, S. O. & Chung, A. S. 2001 Se-methylselenocysteine induces apoptosis mediated by reactive oxygen species in HL-60 cells. *Free Radic. Biol. Med.* **31**, 479–489. (doi:10.1016/S0891-5849(01)00604-9)

38 Abdulah, R., Miyazaki, K., Nakazawa, M. & Koyama, H. 2005 Chemical forms of selenium for cancer prevention. *J. Trace Elem. Med. Biol.* **19**, 141–150. (doi:10.1016/j.jtemb.2005.09.003)

39 Lu, F., Wu, S. H., Hung, Y. & Mou, C. Y. 2009 Size effect on cell uptake in well-suspended, uniform mesoporous silica nanoparticles. *Small* **5**, 1408–1413. (doi:10.1002/smll.200900005)

40 Campayo, L., Grandjean, A., Coulon, A., Delorme, R., Vantelon, D. & Laurencin, D. 2011 Incorporation of iodates into hydroxyapatites: a new approach for the confinement of radioactive iodine. *J. Mater. Chem.* **21**, 17 609–17 611. (doi:10.1039/C1JM14157K)

41 Lavastre, V., Roberge, C. J., Pelletier, M., Gauthier, M. & Girard, D. 2002 Toxaphene, but not beryllium, induces human neutrophil chemotaxis and apoptosis via reactive oxygen species (ROS): involvement of caspases and ROS in the degradation of cytoskeletal proteins. *Clin. Immunol.* **104**, 40–48. (doi:10.1006/clim.2002.5226)

42 Fadeel, B., Ahlin, A., Henter, J. I., Orrenius, S. & Hampton, M. B. 1998 Involvement of caspases in neutrophil apoptosis: regulation by reactive oxygen species. *Blood* **92**, 4808–4818.

43 Kim, A., Oh, J. H., Park, J. M. & Chung, A. S. 2007 Methylselenol generated from selenomethionine by methioninase downregulates integrin expression and induces caspase-mediated apoptosis of B16F10 melanoma cells. *J. Cell Physiol.* **212**, 386–400. (doi:10.1002/jcp.21038)

44 Chen, T. & Wong, Y. S. 2009 Selenocystine induces reactive oxygen species-mediated apoptosis in human cancer cells. *Biomed. Pharmacother.* **63**, 105–113. (doi:10.1016/j.biopha.2008.03.009)

45 Nordberg, J. & Arner, E. S. 2001 Reactive oxygen species, antioxidants, and the mammalian thioredoxin system. *Free Radic. Biol. Med.* **31**, 1287–1312. (doi:10.1016/S0891-5849(01)00724-9)

46 Diaz, B. *et al.* 2008 Assessing methods for blood cell cytotoxic responses to inorganic nanoparticles and nanoparticle aggregates. *Small* **4**, 2025–2034. (doi:10.1002/smll.200800199)

47 Yang, J., Liu, X., Bhalla, K., Kim, C. N., Ibrado, A. M., Cai, J., Peng, T. I., Jones, D. P. & Wang, X. 1997 Prevention of apoptosis by Bcl-2: release of cytochrome c from mitochondria blocked. *Science* **275**, 1129–1132. (doi:10.1126/science.275.5303.1129)

48 Torcia, M. *et al.* 2001 Nerve growth factor inhibits apoptosis in memory B lymphocytes via inactivation of p38 MAPK, prevention of Bcl-2 phosphorylation, and cytochrome c release. *J. Biol. Chem.* **276**, 39 027–39 036.